Energy & Environmental Science

ROYAL SOCIETY OF CHEMISTRY

PAPER

View Article Online
View Journal | View Issue

Cite this: *Energy Environ. Sci.*, 2025, **18**, 7447

Polarity coupling in biphasic electrolytes enables iodine/polyiodide co-extraction for portable Zn–iodine batteries following a liquid–liquid conversion route†

Hai Xu,[ab] Ruanye Zhang,[a] Derong Luo,[a] Kangsheng Huang,[a] Jiuqing Wang,[a] Gengzhi Sun, *[b] Hui Dou *[ac] and Xiaogang Zhang *[ac]

The shuttle effect of polyiodides and aggregation of solid iodine on the cathode surface in aqueous Zn–iodine batteries are considered the main issues for their unsatisfactory cycling stability and slow charge transfer kinetics, respectively. Herein, we develop a biphasic (BP) electrolyte composed of immiscible organic (ethyl acetate, EA) and aqueous solvents for the co-extraction of iodine/polyiodides. The underlying mechanism is clarified by the principle of polarity coupling between iodine species and solvent molecules. Notably, distinct from the formation of solid iodine in an aqueous electrolyte, the electrochemical redox reactions of iodine/polyiodides at the cathodic side (organic phase) investigated by rotating ring electrodes follow the liquid–liquid conversion route. Accordingly, the diffusion of polyiodides is effectively suppressed at the interface of the BP electrolyte and the absence of solid iodine deposition significantly enhances charge transfer kinetics. Moreover, the quasi-solid-state Zn–iodine batteries featuring a gravity-independent stratified architecture are demonstrated, enabled by a BP system consisting of microspace-confined EA and PAM-CMC hydrogel. The fabricated portable device exhibits an areal capacity of 1.40 mA h cm^{-2} at 1 mA cm^{-2}, improved rate performance and stable cycling performance over 22 000 cycles at 10 mA cm^{-2}, indicating extraordinary reliability for wearable applications.

Received 12th May 2025,
Accepted 16th June 2025

DOI: 10.1039/d5ee02593a

rsc.li/ees

Broader context

Recently, Zn–iodine batteries composed of a Zn metal anode and an iodine/host cathode have received worldwide attention because of their Earth-abundance, high theoretical capacities and stable potential plateau. However, the shuttle effect of polyiodides and aggregation of solid iodine on the cathode surface in aqueous Zn–iodine batteries are considered the main issues for their unsatisfactory cycling stability and slow charge transfer kinetics, respectively. Although many effort has been devoted to solving the above issues, there remains a great challenge for the state-of-the-art strategies to simultaneously inhibit polyiodide shuttle and reform the deposition of solid iodine. Herein, we developed a biphasic electrolyte composed of immiscible organic and aqueous solvents for stable Zn–iodine batteries. Specifically, the co-extraction of iodine and polyiodides is experimentally achieved and the mechanism is correlated to the principle of polarity coupling, effectively restricting I-species in the organic phase. Moreover, the electrochemical redox reactions of iodine/polyiodides at the cathodic side (organic phase) following a liquid–liquid conversion route are explored, which are distinct from the formation of a solid iodine passivation layer in an aqueous electrolyte and significantly enhance charge transfer kinetics.

[a] *Jiangsu Key Laboratory of Electrochemical Energy Storage Technologies, College of Materials Science and Technology, Nanjing University of Aeronautics and Astronautics, Nanjing, 210016, China. E-mail: dh_msc@nuaa.edu.cn, azhangxg@nuaa.edu.cn*

[b] *Institute of Advanced Materials, Nanjing Tech University, Nanjing, 211816, China. E-mail: iamgzsun@njtech.edu.cn*

[c] *National Key Laboratory of Mechanics and Control for Aerospace Structures, Institute for Frontier Science, Nanjing University of Aeronautics and Astronautics, Nanjing, 210016, P. R. China*

† Electronic supplementary information (ESI) available. See DOI: https://doi.org/10.1039/d5ee02593a

Introduction

The rapid development of portable/wearable electronics, driven by growing demands of wireless communication, smart human–machine interfaces, artificial intelligence, humanoid robotics and unmanned aerial vehicles, has led to the exploitation of advanced energy storage devices with the expected features of high effectiveness, low-cost and long-serving lifespan.[1–4] Although lithium ion batteries (LIBs) have been commercialized for over 30 years

and are considered the primary choice as the power supply in existing consumable electronics and electric vehicles, the critical challenge in terms of scarce resources of Li-salt undoubtedly hinders their sustainable availability.[5–8] A great amount of effort has been devoted to pursuing alternative substitutions. Among all potential candidates, Zn–iodine batteries composed of a Zn metal anode and an iodine/host cathode receive worldwide attention because of their Earth-abundance, high theoretical capacities and stable potential plateau.[9–12]

In principle, the overall reaction mechanism in Zn–iodine batteries involves the stripping/deposition of the Zn metal anode and the redox of I^-/I^0 following a solid–liquid conversion path.[13–15] At the cathode side, I^- is firstly oxidized to I_2(s) *via* a two-electron transfer process, forming a layer of solid aggregation at the interface between the electrode and the electrolyte; subsequently, I^- needs to cross the solid I_2(s) layer obeying a Grotthuss-like hopping mechanism for further oxidation and unavoidably complex with I_2(s) to produce dissolvable polyiodides (I_3^-, I_5^-, *etc.*). In this whole reaction process, there are two main issues that hinder the development of Zn–iodine batteries:

Firstly, the generated soluble polyiodides at the cathode side will diffuse across the separator to the Zn anode, causing severe corrosion and promoting side reactions, which leads to low Coulombic efficiency and unsatisfactory cycling performance.[16–19] Such a shuttle effect of polyiodides has become the most attractive issue. To address this dilemma, the commonly used strategies are adopting porous carbon as the iodine host material *via* physical adsorption.[20] Nevertheless, special attention to the pore size, structure and distribution is required because of the weak attraction between non-polar carbon and iodine species. By comparison, stronger iodine adsorption can be achieved by organic materials or functional substrates through the chemical bonding of H–I, N–I and O–I.[21–23] However, the loss of active iodine is inevitable after numerous charging/discharging cycles owing to the irreversible formation of the iodine-containing complex.

Secondly, the accumulation of solid iodine with poor electron conductivity (10^{-6} to 10^{-9} S cm^{-1}) generates a passivation layer on the electrode surface, limiting the charge transfer process and slowing down cathodic reactions.[24,25] Although recent efforts have been made to develop highly active electrocatalysts for fast iodine conversion, such as single-atom catalysts,[26] heteroatom-doping[23] and metal–organic frameworks,[27] the aggregation of solid iodine is unavoidable due to its limited solubility in aqueous electrolytes. Therefore, the state-of-the-art strategies face a great challenge to simultaneously inhibit the polyiodide shuttle and reform the deposition of solid iodine.

Alternatively, a biphasic electrolyte (BP) composed of two immiscible solutions, which was primarily applied in redox flow batteries (RFB) to substitute the combination of traditional single-phase electrolytes and ion-exchange membranes, naturally produces an artificial liquid–liquid interface for effectively separating dissolved active species based on their polarities,[28–31] offering a clever tactic to address the abovementioned issues. Recently, the different BP electrolytes of CH_2Cl_2/H_2O,[49] acetonitrile (ACN)/$ZnSO_4$,[50] ACN-ionic liquid/$ZnSO_4$,[51] and ionic liquid/H_2O[52] for Zn–iodine batteries were reported to restrict polyiodides. Nevertheless, the effectiveness of these BP electrolytes in portable Zn–iodine batteries is limited and the detailed reaction mechanism involved in the organic phase remains unexplored. (i) Owing to the reversible and rapid conversion between I_2 and polyiodides, the dissolved polyiodides inevitably contain I_2 components, while it is hard to co-extract I_2 and polyiodides *via* a single solvent owing to their different polarities, which results in inefficient confinement of soluble iodine species through BP systems and the fundamental design principles governing the compatibility between solvents and different iodine species remains unknown; (ii) the cathodic reaction of I^-/I^0 proceeds through a solid–liquid conversion path in aqueous electrolytes, while the unexplored reaction mechanism in the organic phase deserves a detailed study in the BP system; and (iii) the reported BP Zn–iodine/bromine batteries are still prototypes typically in stationary beaker cells, which is impractical for the design of portable/wearable energy storage devices.

Herein, the co-extraction of iodine and polyiodides is experimentally achieved by polarity coupling in a newly developed BP electrolyte for Zn–iodine batteries. In detail, the BP interface is formed between the immiscible organic ethyl acetate (EA) phase containing bis(trifluoromethanesulfonyl)-imide zinc ($Zn(TFSI)_2$) and the aqueous phase of $ZnSO_4$/KI solution, where the dissolved iodine and polyiodides are confined in the organic phase electrolyte (cathode side). The mechanism of co-extraction of iodine/polyiodides is explored and correlated to the principle of polarity coupling between iodine species and solvent molecules. Besides, a liquid–liquid conversion route of iodine at the cathodic side in the BP electrolyte was revealed using a rotating ring electrode (RRE), which is completely distinct from the traditional liquid–solid conversion in aqueous electrolytes, exhibiting much improved charge transfer kinetics. According to these understandings, quasi-solid-state (QSS) portable Zn–iodine batteries featuring a gravity-independent stratified interface based on the BP electrolyte system composed of a microspace-confined EA phase and a PAM-CMC hydrogel further demonstrate superior cycling stability to other reported BP Zn–I/Br batteries. For proof-of-concept applications, the assembled BP devices are successfully employed for health monitoring under multiple practical operation conditions (Fig. 1)

Results and discussion

Iodine (I_2) is a diatomic molecule with a symmetric linear shape. Since both I atoms share an equal proportion of charge, the net dipole moment of I_2 comes out to be zero, making it a nonpolar molecule. As a typical polyiodide, triiodide ion (I_3^-) has a similar linear configuration with no dipole moment in the vapor phase. Nevertheless, the experimental results suggest that I_3^- becomes polarizable and soluble in polar solvents due to the molecule interaction-induced symmetry breaking.[32–35] The differences in polarity make it challenging to co-extract I_2

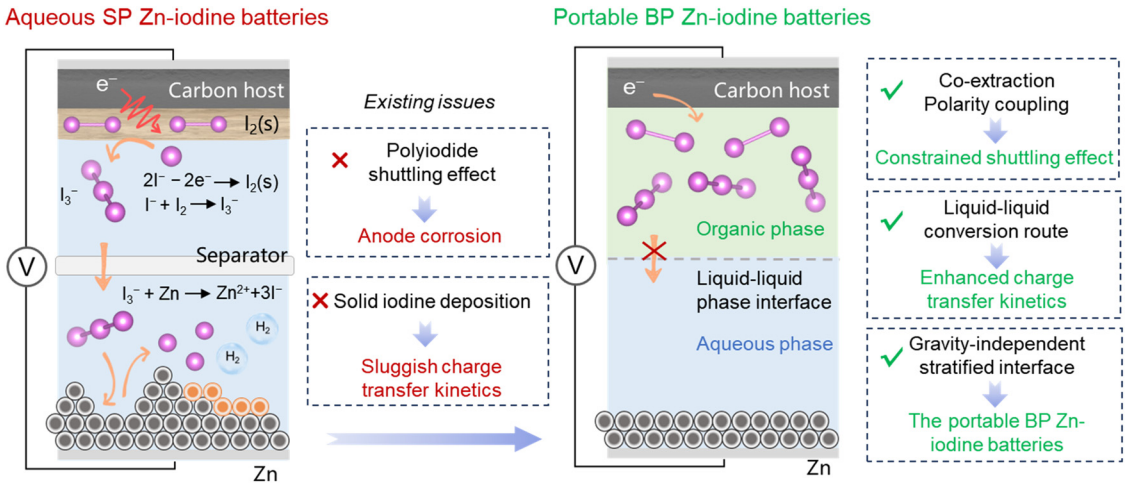

Fig. 1 Schematic diagram of the comparison between aqueous SP Zn–iodine batteries and portable BP Zn–iodine batteries.

and polyiodides according to the principle of "like dissolve like". However, in the application of Zn–iodine batteries, co-extraction is highly necessary because the cathodic reactions involve the reversible electrochemical conversions between I_2 and polyiodides, since dissolved polyiodide species inevitably contain the I_2 components owing to the chemical reaction equilibrium. Unfortunately, the feasibility of constructing a BP electrolyte to restrict I_2/polyiodides on the cathode side *via* a single solvent and prevent their shuttling remains an unknown question to date. In our experiment, an aqueous solution containing I_2 and I_3^- (0.1 M KI/20 mM I_2) was prepared to simulate dissolved iodine species in the aqueous phase and then respectively mixed with a number of solvents with different polarities including petroleum ether (PE), cyclohexane (CH), carbon tetrachloride (CTC), benzene (BZ), ethyl acetate (EA), methyl acetate (MA), pyrrole (Py) and acetonitrile (ACN) (Fig. 2a and b).[36] After a few seconds, self-stratified phases are produced except for the high polar Py and ACN. Notably, the aqueous phase becomes the lightest yellow upon the addition of EA, indicating the nearly complete extraction of polyiodides/iodine. Direct evidence is provided by the ultraviolet-visible (UV-vis) spectra through quantifying the content of I-species respectively in the organic and aqueous phases. Owing to the chemical equilibrium between I_2 and polyiodides, the R value *via* the absorbance changes of I_3^- (288 nm) in the aqueous phase (I_3^- after and I_3^- before) was defined to quantitatively evaluate the extraction ability of different organic solvents for iodine species according to the Lambert–Beer law.

$$R = 1 - \frac{A_{(I_3^- \text{ after})}}{A_{(I_3^- \text{ before})}}$$

As displayed in Fig. 2c, the obvious peaks at ~518 nm of the PE, CH and CTC phases indicate the presence of I_2, corresponding to the violet color of organic phases. The absorption of I_2 blueshifts to ~504 nm in the case of BZ, giving a color of red-brown due to the stronger molecular interaction with electron transfer from an aromatic hydrocarbon to I_2, which is reflected by the newly emerged peak of the BZ–I_2 complex at 288 nm.[37] The corresponding intensity changes of I-species in the UV-vis spectra of the aqueous phase after extraction in Fig. 2d suggest that the non-polar solvents of PE, CH, CTC and BZ exhibit a high selectivity for I_2, while I_3^- cannot be completely extracted into the organic phase with R values of 31%, 35%, 50% and 83% respectively (Fig. 2e). In comparison, both I_3^- (294 and 364 nm) and I_2 (450 nm) are effectively extracted in EA,[38,39] resulting in a calculated R-value of as high as 98%. In the case of MA with a similar structure but slightly increased polarity to EA, only I_3^- is detected in the MA phase with a comparatively decreased R-value of 88%. In addition, the corresponding absorbances of I_3^- (288 nm) in the aqueous phase after extraction by different organic solutions are exhibited in Fig. S1 (ESI†).

The distinct advantages of EA were validated by analyzing the charge distribution and molecular electrostatic potential (ESP). According to the comparison presented in Fig. 3a and Fig. S2 (ESI†), the nonpolar alkyl group and symmetric structure enable the uniform charge distribution in PE, CH, CTC and BZ, while the polar ester group induces the charge separation in EA and MA. Therefore, combined with the experimental results, the principle for the co-extraction of iodine/polyiodides enabled by polarity coupling is summarized in Fig. 3b. The nonpolar PE with hydrophobic alkyl chains ensures efficient extraction of iodine and facilitates the construction of the BP interface, but excludes polyiodides; Py and ACN with strong polarity can homogeneously mix with water, unlikely producing phase separation; EA containing both a nonpolar hydrophobic alkyl group and a polar ester group exhibits moderate molecule polarity and allows the formation of a self-stratified BP system with water and simultaneous extraction of iodine and polyiodides. As a control experiment, although MA possesses a similar structure to EA, the slightly increased polarity due to the shortened alkyl chain limits the ability to extract iodine, further validating the principle of polarity coupling.

More compelling evidence was obtained through an experiment investigating the difference between the non-polarity and polarity groups in extracting the I_2 aqueous solution and the I_3^-

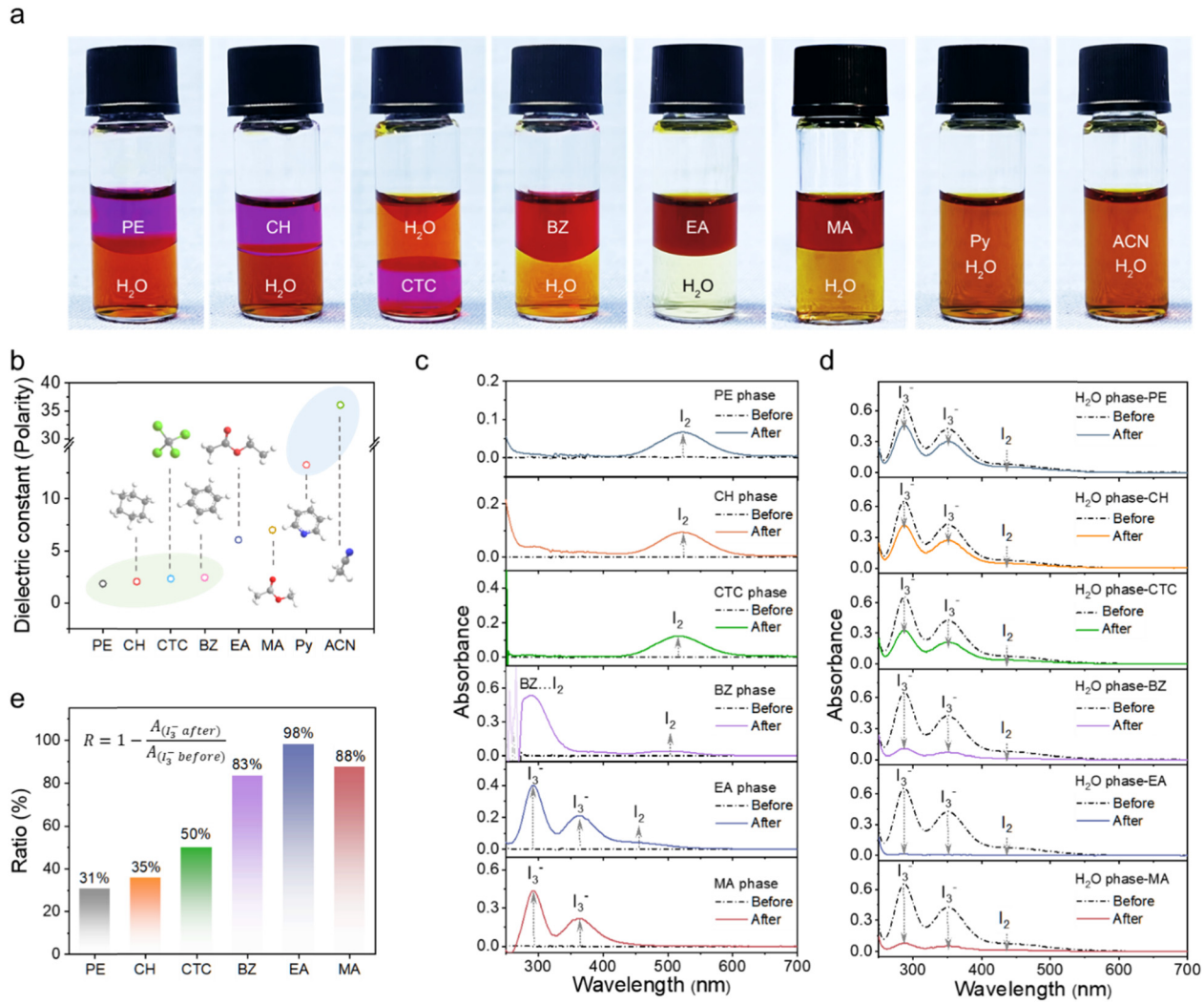

Fig. 2 Selection of organic solvents and extraction effects of iodine and polyiodides. (a) The photos of different BP extract systems composed of the organic phase (PE, CH, CTC, BZ, EA, MA, Py and ACN) and 0.1 M KI/20 mM I_2 aqueous phase. (b) The dielectric constants of different organic solvents. The UV-vis spectra of (c) different organic phases and (d) the 0.1 M KI/20 mM I_2 aqueous phase before and after extraction. (e) *R* value of I_3^- peaks of the H_2O phase after extraction.

aqueous solution. The I_3^- aqueous solution was prepared by mixing 0.1 M KI and 1 mM I_2; excess KI ensures the nearly complete conversion of I_2 to I_3^-. The I_2 aqueous solution was obtained by ultrasonication of solid iodine in water. As shown in Fig. 3c, PE, EA and MA were mixed with the I_3^- aqueous solution and I_2 aqueous solution, respectively, spontaneously producing self-stratified phases. Taking solution color, *R*-value and the corresponding absorbance changes into consideration (Fig. 3d–g and Fig. S3, ESI†), it is reasonable to conclude that PE exhibits excellent extraction efficiency for I_2 but weak extraction for I_3^-. Conversely, MA displays good ability for extracting I_3^- together with moderate extraction efficiency for I_2. These results suggest that polar and non-polar functional groups in organic molecules function differently in their tendencies to extract I_2 and I_3^-, Notably, EA demonstrates exceptional capability in extracting I_2 and I_3^- from aqueous solutions because of its well-suited polarity coupling.

Molecular dynamics (MD) simulations were also conducted to investigate the co-extraction ability of the EA-H_2O BP system for I_3^- and I_2 (Fig. S4, ESI†). I_3^- and I_2 distributed in the H_2O phase in the initial state rapidly diffuse to and fully fill in the EA phase in the final state, suggesting the strong interaction between I_2/I_3^- and EA. This was further proved by DFT calculations (Fig. S5, ESI†). According to molecular orbital theory, an empty antibonding (σ^*) orbital is formed in I_2 and I_3^- molecules due to the unique outermost electronic configuration of $5s^25p^5$ in the I atom (Fig. S6, ESI†),[40,41] which is prone to accept the donated lone-pair electrons from the negatively charged C═O/C–O. Such a charge transfer behavior between EA and I_3^-/I_2 is clearly evidenced in the optimized charge-density-difference pattern (Fig. S7, ESI†).

In order to ensure that the ionic conductivity of the EA phase was high enough, $Zn(TFSI)_2$ was selected as the Zn-salt because the other commonly used ones such as $Zn(ClO_4)_2$, $ZnSO_4$ and

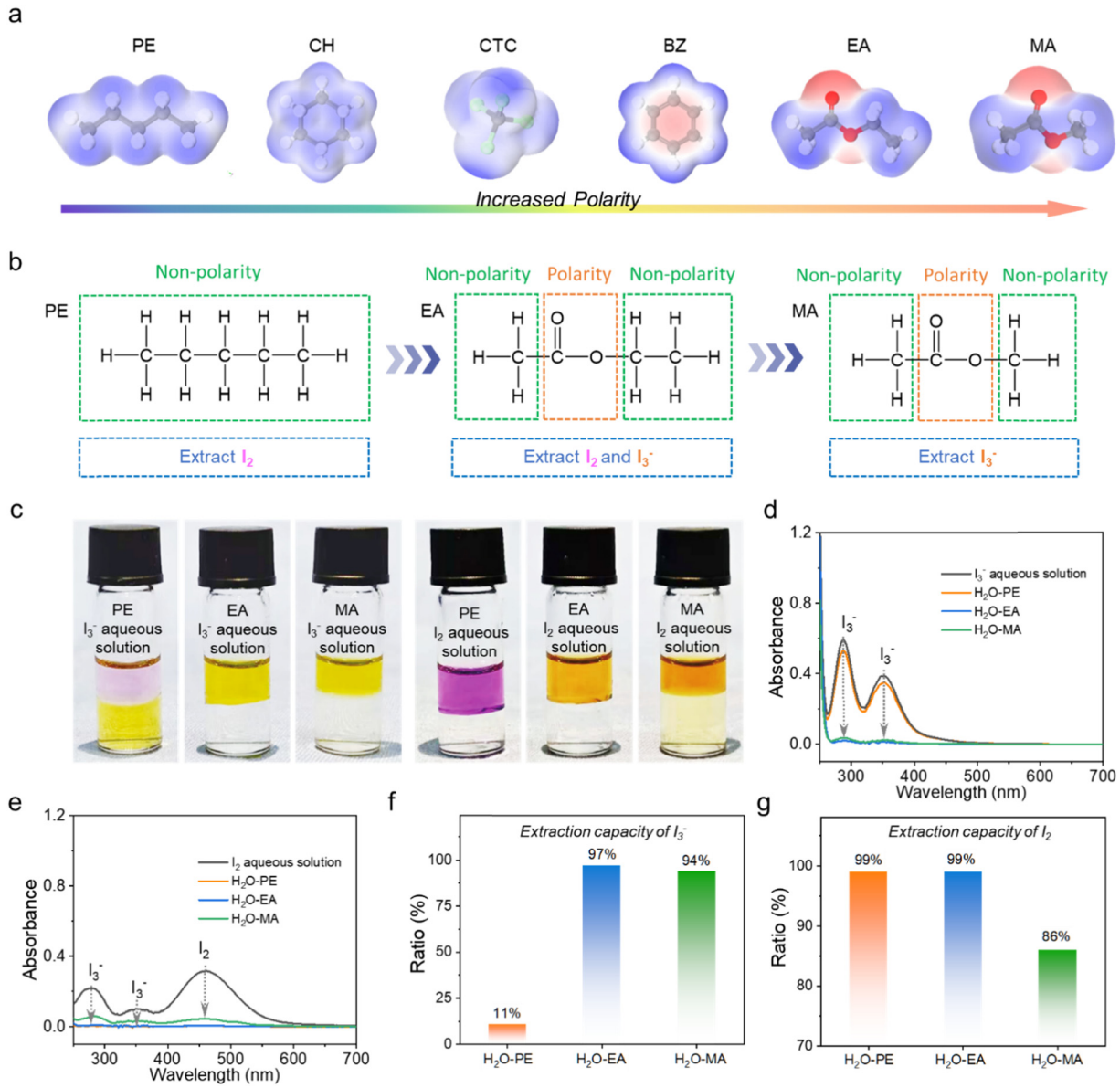

Fig. 3 (a) Electrostatic potential distribution of different solvents. (b) The relationship between molecular polarity and iodine species extraction. (c) The photos of different BP extract systems composed of the organic phase (PE, EA, and MA) and I_3^- and I_2 aqueous phase. (d) and (e) The UV-vis spectra of different aqueous phases before and after extraction. (f) and (g) *R* values of I_3^- peaks (288 nm) and I_2 peaks (460 nm) of the aqueous phase after extraction.

$Zn(OTf)_2$ cannot be dissolved in EA due to their relatively strong interaction between the anion and cation (Fig. S8, ESI†). Consequently, an immiscible BP electrolyte system was successfully prepared by simply mixing 1 M $Zn(TFSI)_2$ in EA and an aqueous solution containing 1 M $ZnSO_4$ + 0.5 M KI (Fig. S9, ESI†). The ion conductivity of the obtained upper EA (1 M $Zn(TFSI)_2$) phase is found to be 14.34 mS cm^{-1} (Fig. S10, ESI†), better than most of the reported values for organic electrolytes even though still lower than that of the bottom aqueous solution (76.41 mS cm^{-1}).

The redox behavior of iodine in the BP electrolyte system is revealed in a visualized two-electrode system with a glass carbon (GC) as the cathode inserted in the EA phase (1 M $Zn(TFSI)_2$) and a Zn rod as the anode in the aqueous phase (1 M $ZnSO_4$ + 0.5 M KI) (Fig. S11, ESI†). Chronoamperometry (CA) was adopted by respectively applying 1.4 V and 0.4 V for 250 s to oxidize and reduce I-species. In the corresponding current–time curve (Fig. 4a), four representative points of A, B, C and D are selected for the subsequent acquisition to characterize the chemical composition of the resultant products. As shown in Fig. 4b, yellow polyiodides emerge on the surface of the GC electrode and then gradually dissolve in the EA phase during the electrochemical oxidation from A to C. Upon switching the polarization voltage to 0.4 V, the color of the EA phase continuously fades from the C to the D state attributable to the reduction of polyiodides. It is noted that the bottom aqueous

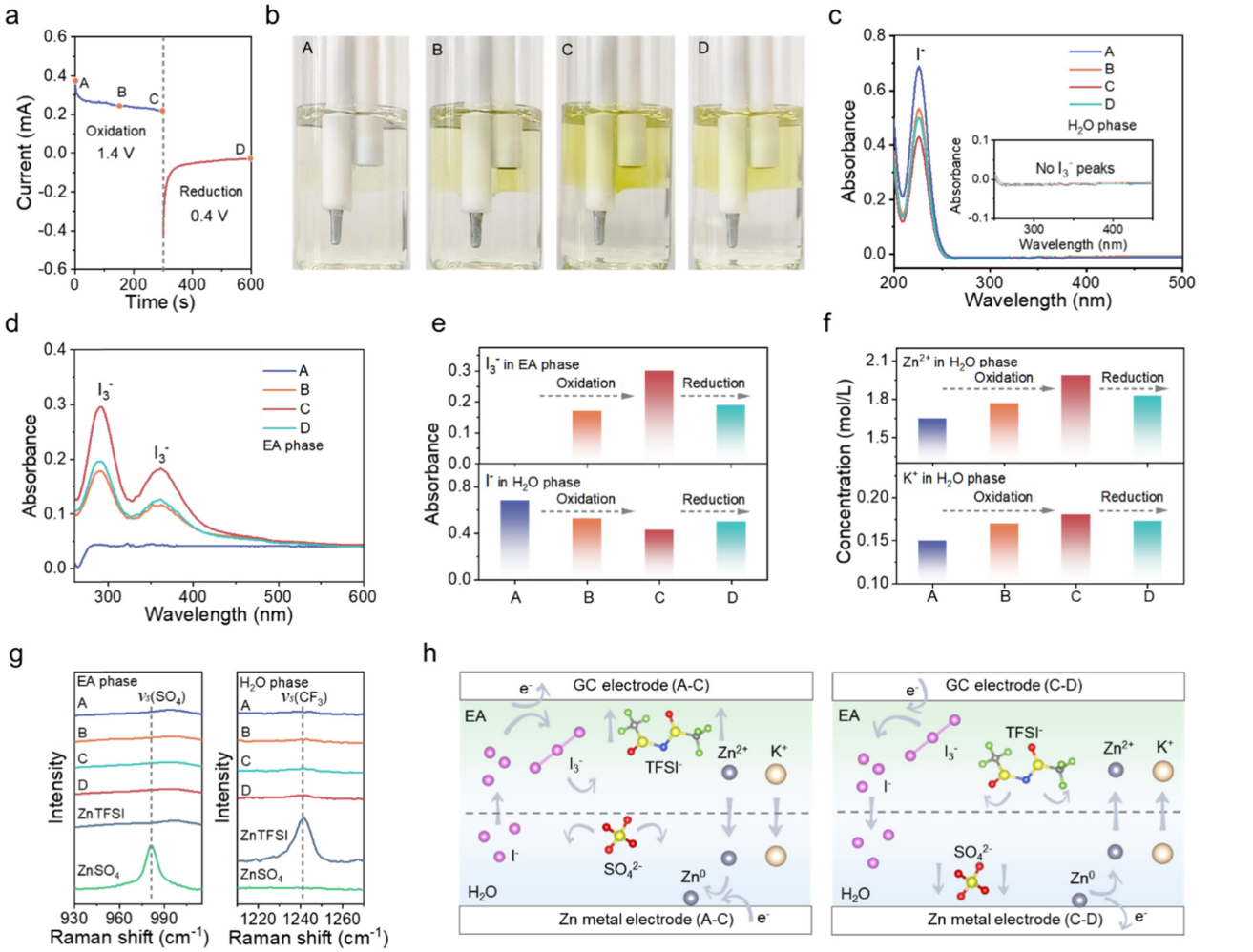

Fig. 4 Characterization of the ion transport behavior across the interface of the BP electrolyte. (a) The CA curves marked with four represented states (A, B, C and D). (b) The digital photos of the visualized two electrode system corresponding to the states of A–D. The UV-vis spectra in the states of A–D of (c) the EA phase and (d) the H_2O phase. The summarized (e) UV-vis absorbance changes of I_3^- in the EA phase and I^- in the H_2O phase and (f) concentration changes of Zn^{2+} and K^+ in the H_2O phase from states A to D. (g) The Raman spectra of the EA phase and the H_2O phase in the states of A–D, 1 M $ZnSO_4$ in H_2O and 1 M $Zn(TFSI)_2$ in EA. (h) The schematic of the ion transport mechanism during the charging–discharging process.

phase remains colorless during the whole process, suggesting the effective inhibition of polyiodide shuttling. Comparably, in the single phase (SP) aqueous electrolyte (1 M $ZnSO_4$ + 0.5 M KI), once the polyiodides are generated, they freely diffuse to the anode side without any restriction (Fig. S12, ESI†). The UV-vis spectra provide direct evidence for the concentration variation of I^- and I_3^- in the organic and aqueous phases (Fig. 4c and d). In the aqueous phase, the content of I^- gradually decreases under oxidation and increases at reduction, without any discernible signal from I_3^- during the entire process. Oppositely, in the organic phase, the content of I_3^- gradually increases in the process of oxidation from state A to C and decreases in the process of reduction from state C to D. The UV-vis absorbance of I^- in the H_2O phase and that of I_3^- in the EA phase in the different states are summarized in Fig. 4e. Therefore, it could be concluded that I^- can cross the BP interface and be oxidized at the GC surface, whereas the produced polyiodides are thoroughly restrained in the organic phase.

Additionally, inductively coupled plasma mass spectrometry (ICP-MS) and Raman spectra were further utilized to monitor the transport of ions involved in the charging–discharging process. In Fig. 4f, the concentrations of K^+ and Zn^{2+} in the aqueous phase increase from states A to C and then decrease from C to D according to the ICP-MS results, indicating the migration of Zn^{2+} and K^+ across the BP interface. Moreover, Raman spectra show typical vibration peaks of S=O at 980 cm^{-1} and C–F at 1240 cm^{-1}, respectively ascribing to SO_4^{2-} and $TFSI^-$.[42–44] The results displayed in Fig. 4g indicate that SO_4^{2-} in the aqueous phase and $TFSI^-$ in the organic phase are not able to cross the BP interface even under an electric field. Based on the above analysis, the ion transport mechanism can be concluded in Fig. 4h. From state A to C, Zn^{2+} and K^+ migrate to the anode side, where Zn^{2+} accepts the electrons and is reduced to Zn^0; I^- moves to the cathode side and is oxidized to generate polyiodides and iodine. Once the polarization voltage is switched to 0.4 V, Zn metal is dissolved

in the aqueous phase and I_3^- restrained in EA is reduced to I^-, accompanied by the diffusion of Zn^{2+} and K^+ to the cathode side and I^- to the anode side. Besides, $TFSI^-$ and SO_4^{2-} do not cross the BP interface during the charge–discharge process, although they diffuse under the electric field.

In principle, the cathodic reactions of Zn–iodine batteries involve the electrochemical conversion of I^-, the complexation between I^- and I_2(s), and the formation of polyiodides in the charging process, which are difficult to detect by traditional spectroscopic techniques. A viable strategy to explore the reaction mechanism that occurred at the electrode/electrolyte interface is to use a rotating ring disk electrode (RRE: GC disk and Pt ring in this study) as the working electrode, coupled with Ag/AgCl as the reference electrode and Pt plate as the counter electrode (Fig. S13, ESI†). Experimentally, SP and BP were respectively utilized as electrolytes, a potential of 0–0.7 V was applied at the GC disk, and a constant potential of 0.2 V was held at the Pt ring to reduce the iodine species, with the rotation speed of the RRE maintained at 150 rpm.

Fig. 5a shows the linear sweep voltammetry (LSV) curves for the oxidation of I^- in the SP electrolyte, which can be divided into four distinct regions: region-I 0–0.48 V, region-II 0.48–0.5 V, region-III 0.5–0.53 V and region-IV 0.53–0.7 V. In region-I, the oxidative current (denoted as i_o) at the GC disk corresponding to the conversion from I^-(aq) to I_3^-(aq) through the soluble I_2(aq) and reductive current (denoted as i_r) of the conversion from I_3^-(aq) to I^-(aq) at the Pt ring grow synchronously following the reactions (1) and (2).

$$3I^-(aq) - 2e^- \leftrightarrows I_2(aq) + I^-(aq) \leftrightarrows I_3^-(aq) \quad (1)$$

$$I_3^-(aq) + 2e^- \leftrightarrows 3I^-(aq) \quad (2)$$

The accumulation of I_2(aq) in the vicinity of the GC disk leads to the precipitation of solid I_2(s) upon further increase in

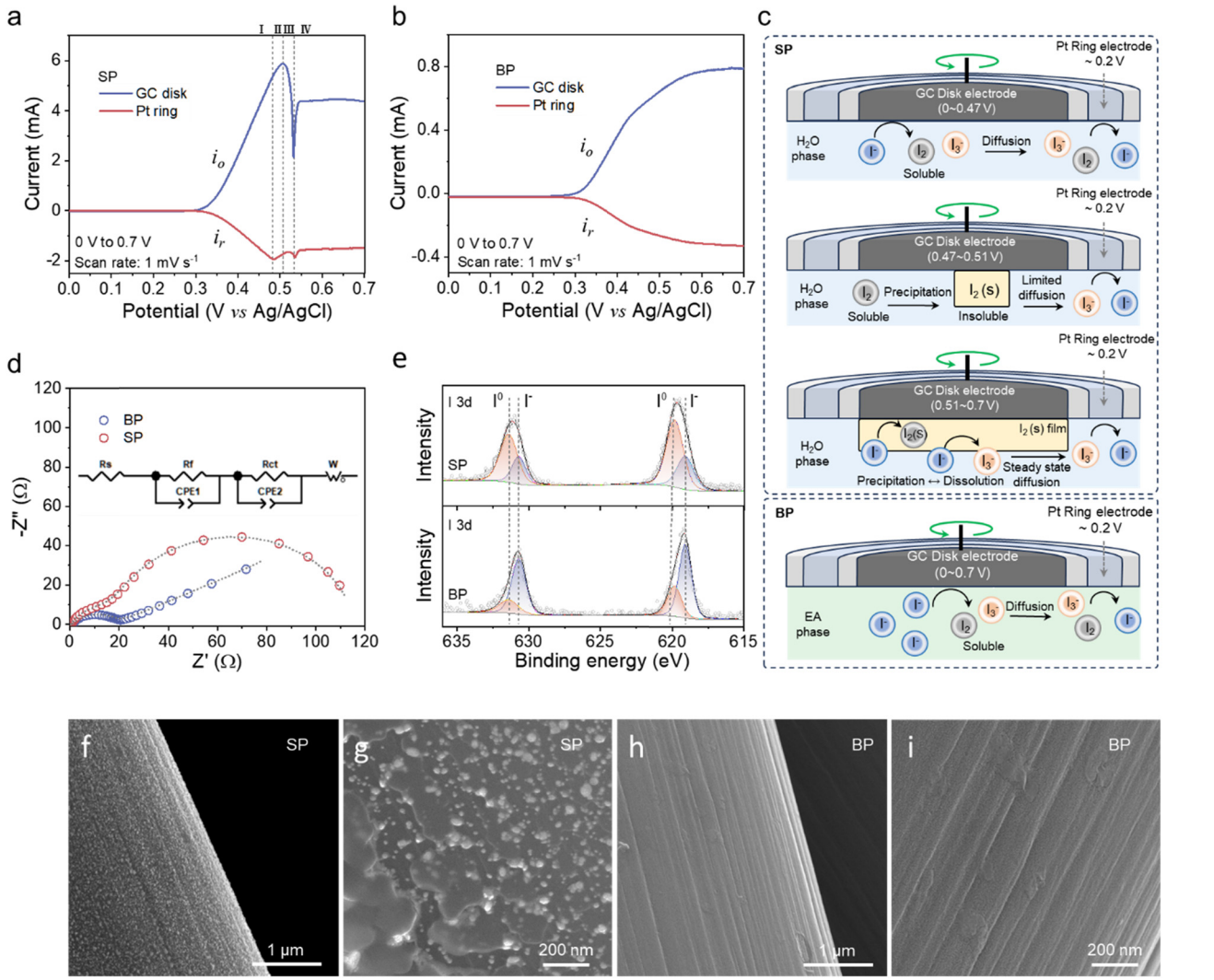

Fig. 5 Characterization of the cathodic reactions in the BP and SP electrolytes. LSVs on RRE in the (a) SP and (b) BP electrolytes from 0 V to 0.7 V. (c) The schematic of redox reactions at the interface between the electrode and the electrolyte. (d) The EIS plots, (e) XPS spectra and (f)–(i) SEM images of the CC cathode for coin cells based on BP and SP after 15 s polarization under 1.5 V.

the potential owing to its limited solubility in the aqueous electrolyte as the equilibrium shown in reaction (3).

$$I_2(aq) \leftrightarrows I_2(s) \quad (3)$$

The precipitated $I_2(s)$ on the GC disk cannot transport to the Pt ring, thus i_r gradually decreases in region-II. Subsequently, further aggregation of $I_2(s)$ on the GC disk slows down the oxidation reaction caused by the limited ion diffusion, even though the partial dissolution of $I_3^-(aq)$ occurs as depicted in reaction (4), thus leading to a dramatically decreased i_o and thereafter an increased i_r in region-III.

$$I_2(s) + I^-(aq) \leftrightarrows I_3^-(aq) \quad (4)$$

When the formed $I_2(s)$ layer completely covers the surface of the GC disk, i_o reaches the lowest point and the manner of $I^-(aq)$ transport changes from direct diffusion to "carrier"-type diffusion according to the Grotthuss mechanism through the $I_2(s)$ film. Finally, both i_o and i_r reach the steady-state in region-IV, indicating that the dissolution–precipitation of the $I_2(s)$ film attains the equilibrium state. The above analysis supports the solid–liquid reaction route which is in good accordance with our previous work.[12] Comparably, in the case of BP electrolyte, i_o and i_r monotonously increase and ultimately reach the equilibrium state with the applied potential (Fig. 5b), indicating a totally different reaction mechanism from that in the aqueous SP electrolyte without the presence of $I_2(s)$ owing to the high dissolubility of both I_2 and polyiodides in EA following the so-called liquid–liquid conversion route. Such a special mechanism is confirmed by LSV from 0.7 V to 0 V in Fig. S14 (ESI†), where a peak attributable to the decomposition of the $I_2(s)$ film occurs in the SP system rather than in the BP system. The abovementioned reaction mechanisms in SP and BP electrolytes are summarized in Fig. 5c and Fig. S15 (ESI†) based on the principle that EA with moderate polarity possesses much higher solubility of both I_2 and polyiodides than H_2O, avoiding the aggregation of $I_2(s)$ and realizing the liquid–liquid conversion.

In order to further validate the above mechanism, the coin cells assembled with the Zn anode and carbon cloth (CC) cathode separately in BP and SP electrolytes were characterized by the CA technique at 1.5 V for 30 s and then their electrochemical impedance spectroscopy (EIS) results are displayed in Fig. 5d. Obviously, the wide semicircle in the intermediate/low frequency region for the batteries based on the SP electrolyte suggests an extra barrier resistance owing to $I_2(s)$ precipitation. Direct evidence can be found in the I 3d XPS spectra (Fig. 5e) and SEM images (Fig. 5f–i) of the CC cathode,[45,46] where a stronger I^0 signal is obtained and apparent $I_2(s)$ particles present on the cathode disassembled from the SP-based batteries but not with the BP-based batteries, verifying that the cathodic reactions in the BP electrolyte follows a different liquid–liquid reaction mechanism.

Although the feasibility of the BP electrolyte in prohibiting polyiodide shuttling and the reaction mechanism of I-species in the organic phase have been validated theoretically and experimentally, challenges still remain in the construction of portable Zn–iodine batteries. Firstly, the long diffusion distance of dissolved polyiodides in organic electrolytes leads to an irreversible charging/discharging process (Fig. 4b). Secondly, the gravity-driven stratification is inadequate for complex operational environments. We therefore proposed a QSS portable Zn–iodine battery based on a gravity-independent stratified interface realized by a synergistic effect between a microspace-confined EA phase in an activated carbon (AC) cathode and hydrogel as an aqueous phase to address the above issues (Fig. 6a). With AC serving as an effective cathode host, its ultra-high specific surface area ($\sim$2198 $cm^2\ g^{-1}$) and organophilic properties enable the rapid absorption of the EA electrolyte, and the abundant mesopores (10–20 Å) also could function as reaction micro-vessels, immensely shortening the diffusion distance of dissolved polyiodides and avoiding irreversible redox reactions (Fig. S16 and S17, ESI†). On the other hand, a hydrogel containing 1 M $ZnSO_4$/0.5 M KI is prepared by chemically crosslinking polyacrylamide and carboxymethyl cellulose (PAM-CMC) (Fig. S18, ESI†), in which water molecules are constrained in the polymeric network, guaranteeing efficient ion diffusion and at the meantime further limiting the diffusion of iodine species. As displayed in Fig. 6b, after 24 h, the added I_3^-/I_2 are effectively constrained in the EA phase, leaving hydrogel colorless, whereas severe shuttling of I_3^- was observed in the water//hydrogel SP system. When PAM-CMC and the EA phase were sequentially vialed in a bottom-up manner, forming a distinct interface, it can remain intact upon flipping over and keep stable even after 30 days (Fig. 6c and Fig. S19, ESI†). Combining with the advantages of the AC cathode and PAM-CMC hydrogel, the QSS devices were assembled in the configuration Zn//hydrogel//AC-EA based on the above BP electrolytes and then electrochemically evaluated at a constant current of 0.5 mA cm^{-2}. *In situ* Raman spectra confirm the highly reversible reactions at the cathode side with the appearance and disappearance of I_3^- at 110 cm^{-1} and I_5^- at 160 cm^{-1} respectively in the charging and discharging processes (Fig. 6d). Moreover, almost the same GCD curves at 1 mA cm^{-2} with a high coulombic efficiency of 98.6% are obtained no matter how the batteries work in the way of anode upward or cathode upward, further ensuring the effectiveness of the design for gravity-independent BP-based energy storage systems (Fig. S20, ESI†).

In our previous study,[13] it has been proved that the side reactions occurring at the Zn anode mainly originate from the corrosion by dissolvable polyiodides, resulting in a highly porous and loose surface which subsequently accelerates the hydrogen evolution reaction (HER), consumes protons in the aqueous electrolyte, and locally induces the precipitation of $Zn_4SO_4(OH)_6{\cdot}xH_2O$ (Fig. 7a). Herein, the anodes respectively disassembled from the batteries of Zn//hydrogel//AC (SP) and Zn//hydrogel//AC-EA (BP) after 10 cycles at 0.5 mA cm^{-2} were characterized to verify the suppression to the side reactions by the BP electrolyte *via* restricting the shuttle of polyiodides. The stronger XRD signals ascribed to $Zn_4SO_4(OH)_6{\cdot}xH_2O$ in the SP electrolyte reveal the more severe corrosion that occurred at the

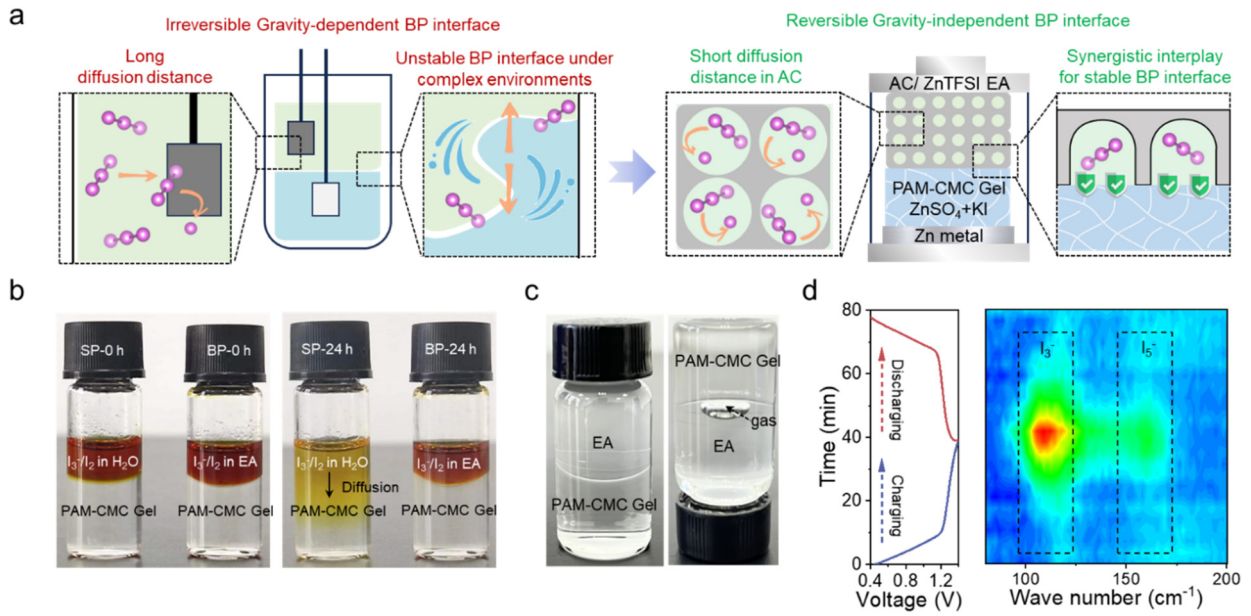

Fig. 6 (a) The design of gravity-dependent and gravity-independent BP interfaces. (b) The photos for the shuttle experiment of I_3^-/I_2 in EA/PAM-CMC (BP) and H_2O/PAM-CMC (SP) systems. (c) The photos of gravity-independent test of EA/PAM-CMC. (d) The *in situ* Raman spectra of Zn–iodine based on the BP electrolyte during the charging/discharging process.

Zn anode in comparison with that in the BP electrolyte (Fig. 7b and Fig. S21a, ESI†). SEM images also confirm the severe corrosion of the Zn anode in the SP electrolyte with more platelets generated on the surface (Fig. 7c and d and Fig. S21b, ESI†). The composition of the cycled Zn anodes was analyzed in depth direction using X-ray photoelectron spectroscopy (XPS) equipped with an etching technique (Fig. 7e and 7f). The platelets can be identified as $Zn_4SO_4(OH)_6{\cdot}xH_2O$ with the characteristic peaks of Zn^{2+} at 1023.1 eV and SO_4^{2-} at 169.8 eV at the outermost layer of Zn anodes.[22,47,48] It is noteworthy that, according to the emergence of XPS signals of Zn^0 and disappearance of SO_4^{2-}, the corrosion depths of the Zn anode disassembled from the BP and

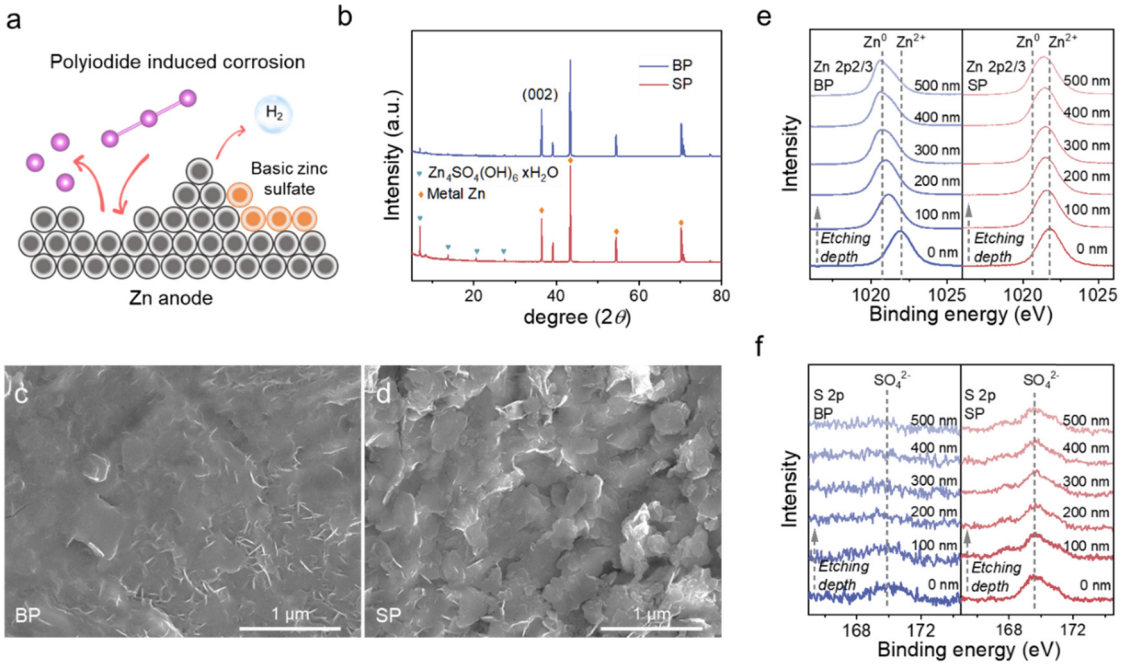

Fig. 7 Characterization of the anode in BP and SP electrolytes. (a) The schematic diagram of polyiodide-induced corrosion at the Zn anode surface. (b) The XRD patterns, (c) and (d) SEM images and the etching XPS results of (e) Zn $2p_{2/3}$ and (f) S 2p of Zn electrodes after 50 cycles in the Zn–iodine batteries based on the BP and SP electrolytes.

SP batteries vary significantly with 100 nm and 500 nm respectively, demonstrating that the co-extraction of iodine and polyiodides in BP effectively inhibits the side reactions of corrosion and hydrolysis and thereby guarantees a relatively stable electrolyte/anode interface.

The electrochemical performances of QSS Zn–iodine batteries respectively based on the BP and SP electrolytes were fully evaluated. The CV curves at 0.1 mV s^{-1} display similar shape and characteristic redox peaks of iodine, yet different voltage gaps between the anodic and cathodic peaks for the BP (0.20 V) and SP (0.25 V) electrolytes (Fig. 8a). Moreover, the anodic peak respectively shifts 80 and 110 mV for BP and SP devices when the scan rate increases from 0.2 mV s^{-1} to 1 mV s^{-1} (Fig. S22, ESI†). Both the large voltage gap and anodic peak shift in the SP electrolyte are ascribed to the slow electron transfer caused by the formation of solid iodine precipitation. As a consequence, the batteries based on the BP electrolyte deliver an areal capacity of 1.40 mA h cm^{-2} at 1 mA cm^{-2} and retain 0.75 mA h cm^{-2} at 10 mA cm^{-2} with a superior retention of 54% compared to 38% of the SP device (Fig. 8b). Besides, the relatively higher mid-discharge voltages at different current densities further demonstrate the fast redox reactions and stable electrode/electrolyte interface in the BP system (Fig. 8c and d and Fig. S23, ESI†). The optimized energy/power densities

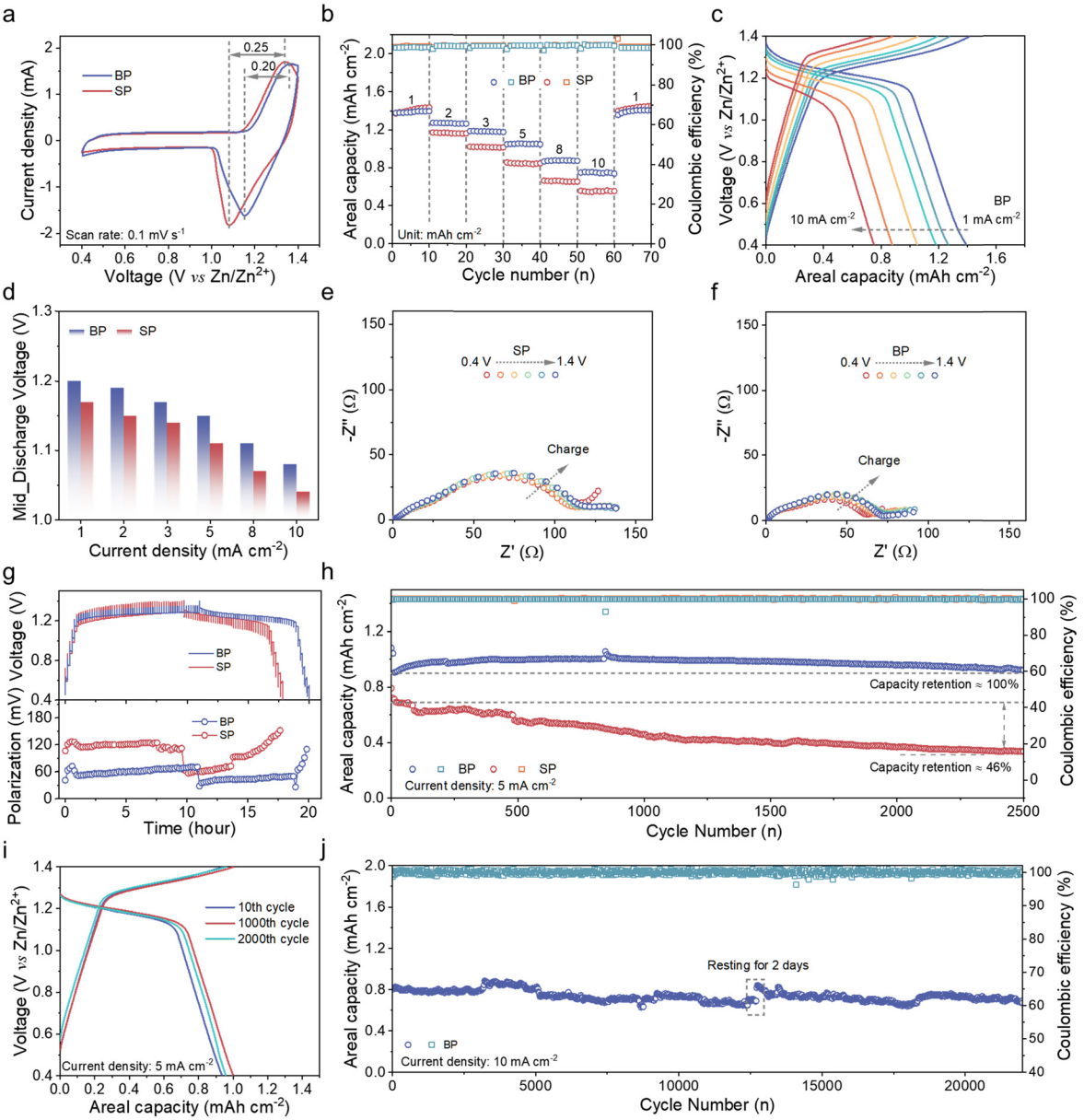

Fig. 8 The electrochemical performances of QSS Zn–iodine batteries based on the BP and SP electrolytes. (a) The CV curves at 0.1 mV s^{-1}. (b) The rate performance. (c) The GCD curves of the BP electrolyte at different current densities. (d) The mid-discharge voltages. (e) and (f) The *in situ* EIS spectra during the charging process. (g) The GITT curves. (h) The cycling performance at 5 mA cm^{-2}. (i) The GCD curves of the BP electrolyte at 5 mA cm^{-2}. (j) The cycling performance of the BP electrolyte at 10 mA cm^{-2}.

of 1.52 mW h cm^{-2} (at 1.1 mW cm^{-2}) and 9.73 mW cm^{-2} (at 0.73 mW h cm^{-2}) are achieved for Zn–iodine batteries based on the BP electrolyte (Fig. S24, ESI†).

The *in situ* EIS tests monitor the resistance changes of QSS Zn–iodine batteries (Fig. 8e and f). Owing to the absence of a solid iodine layer, the device based on the BP electrolyte demonstrates a much lower charge transfer resistance than that based on the SP electrolyte during the charging process, realizing faster reaction kinetics. As displayed by the galvanostatic intermittent titration technique (GITT), the BP device shows a smaller voltage fluctuation due to the minimized polarization in comparison with the SP device (Fig. 8g), which agrees well with the results from EIS. Benefiting from the restriction of polyiodides and regulation of the cathode surface in the BP electrolyte, the assembled cell exhibits significantly enhanced stability with similar GCD curves at the 10th, 1000th and 2000th cycles, achieving a 100% areal capacity retention over 2500 cycles at a current density of 5 mA cm^{-2} (Fig. 8h and i). Even at a high current density of 10 mA cm^{-2}, the batteries exhibit outstanding cycling stability over 22 000 cycles (Fig. 8j), which is superior to other reported BP Zn–I/Br batteries (Tables S1 and S2, ESI†), indicating great potential to meet the requirements under practical conditions.

The QSS pouch cells (3 cm × 4 cm) of Zn anode//hydrogel// AC-EA cathode with CC current collector were also fabricated in an aluminum-plastic package. The QSS pouch cells output areal capacities of 1.45, 1.33, 1.26, 1.20 and 1.15 mA h cm^{-2} with a high coulomb efficiency of ~100% at 10, 20, 30, 40, and 50 mA, respectively (Fig. 9a and b). The calculated maximum energy density reaches 1.59 mW h cm^{-2}. Benefiting from the special design, the pouch cell exhibits excellent environmental adaptability with 100%, 96% and 98% capacity retentions as the device was inverted, bent (90°), and hammered (20 times) (Fig. 9c and d). When the cell was cycled in a 100% depth of discharge for 450 h (Fig. 9e), it still can sustain negligible capacity loss with an average coulomb efficiency of 99.5% (Fig. 9f). Besides, such a device maintains stability over 30 cycles of 90° bending–unbending, suggesting its excellent mechanical reliability (Fig. S25, ESI†). The portable QSS pouch cells were further integrated with a wearable sensing system for continuous health monitoring. In detail, three QSS pouch cells connected in series offer the capability to safely power a smart watch that can acquire the corresponding data of heart beat and blood pressure (Fig. 9g). The tandem device mounted on human limb maintains stable operation under various movements.

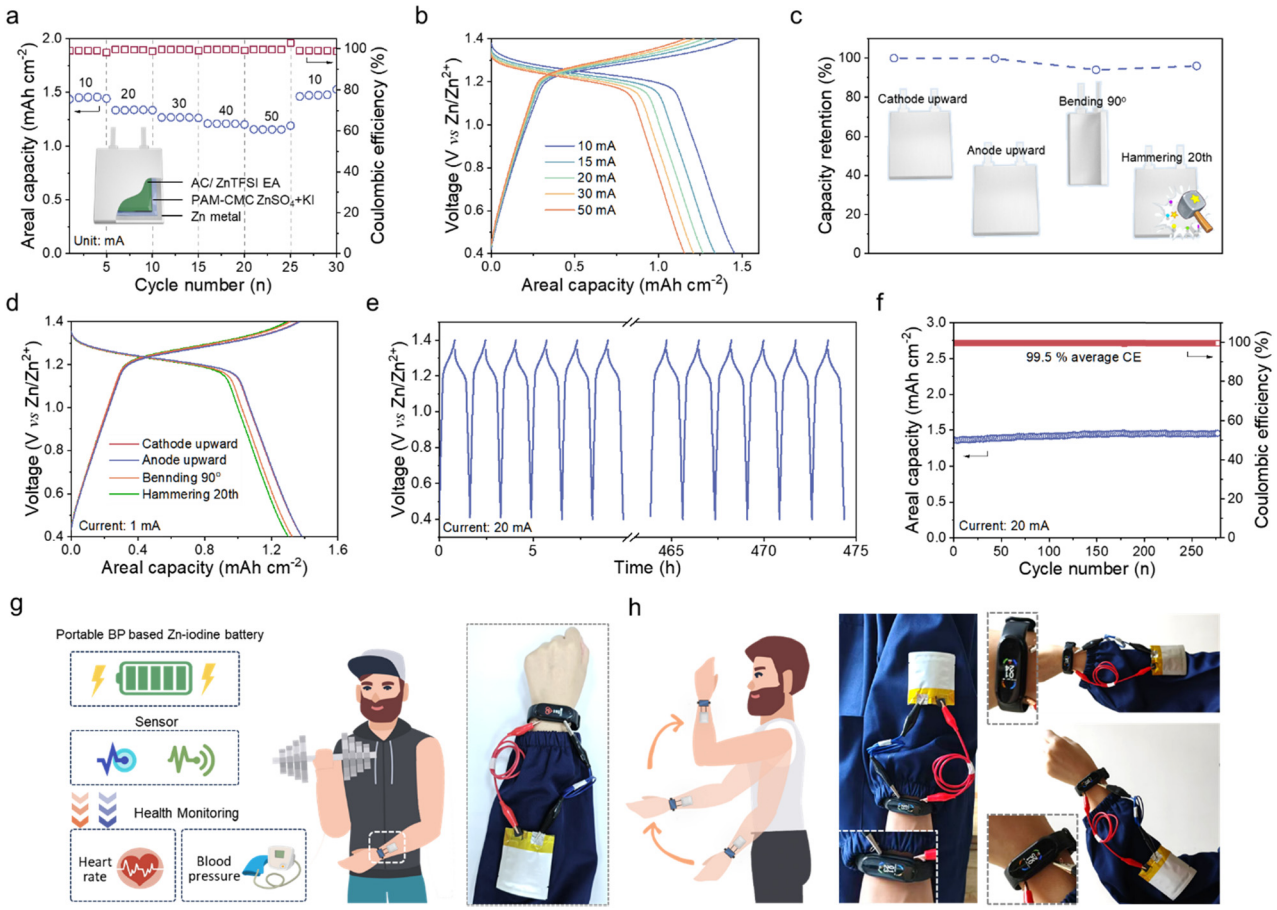

Fig. 9 The performance of the QSS pouch cells based on the BP electrolyte. (a) The rate performance. (b) The GCD curves from 10 mA to 50 mA. (c) The capacity retention and (d) GCD curves under different working conditions. (e) The voltage–time curves and (f) cycling performance at 20 mA. (g, h) Schematic diagram of an integrated portable energy storage-sensing system and demonstration photos of health monitoring.

These application measurements demonstrate the feasibility of our rational design for daily usage and potential in a broader context (Fig. 9h).

Conclusions

In summary, we developed a BP electrolyte system composed of two immiscible solutions of $Zn(TFSI)_2$ in EA and $ZnSO_4$/KI in water to address the key issues of Zn–iodine batteries. Due to the proper nonpolar hydrophobic alkyl chain and polar ester groups, EA with moderate molecule polarity shows the polarity coupling with iodine species, and it allows the formation of a self-stratified BP system with water and simultaneous extraction of iodine and polyiodides, effectively preventing the shuttling effect of polyiodides. More importantly, multiple spectral characterization methods and electrochemical testing disclose that the cathodic reactions follow an unconventional liquid–liquid conversion route without the formation of a solid iodine passivating layer, achieving much faster charge transport kinetics. The designed QSS portable Zn–iodine battery with a gravity-independent stratified interface based on the BP electrolyte with microspace-confined EA and PAM-CMC hydrogel exhibits an enhanced areal capacity of 1.40 mA h cm^{-2} at 1 mA cm^{-2}, excellent rate performance of 0.75 mA h cm^{-2} at 10 mA cm^{-2}, 100% capacity retention after 2500 cycles at 5 mA cm^{-2} and cycling stability of over 22 000 cycles at 10 mA cm^{-2}. As proof-of-application, the assembled pouch cell based on the BP electrolyte can adapt to complex operation environments and realize energy storage supply for human health monitoring.

Author contributions

The manuscript was written through contributions of all authors. All authors have given approval to the final version of the manuscript.

Conflicts of interest

There are no conflicts to declare.

Data availability

Data are available upon request from the authors.

Acknowledgements

This work was supported by the National Key Research and Development Project Intergovernmental International Science and Technology Innovation Cooperation (2022YFE0109400), the National Key Research and Development Program of China (2023YFB2405800) and the Leading Edge Technology of Jiangsu Province (BK20232022 and BK20220009). This work was supported by the facilities in the Center for Microscopy and Analysis at Nanjing University of Aeronautics and Astronautics.

References

1 S. Ding, T. Saha, L. Yin, R. Liu, M. I. Khan, A.-Y. Chang, H. Lee, H. Zhao, Y. Liu and A. S. Nazemi, *Nat. Electron.*, 2024, **7**, 1–12.
2 C. Lu, H. Jiang, X. Cheng, J. He, Y. Long, Y. Chang, X. Gong, K. Zhang, J. Li and Z. Zhu, *Nature*, 2024, **629**, 1–6.
3 S. Saifi, X. Xiao, S. Cheng, H. Guo, J. Zhang, P. Müller-Buschbaum, G. Zhou, X. Xu and H.-M. Cheng, *Nat. Commun.*, 2024, **15**, 6546.
4 K. Zhang, X. Shi, H. Jiang, K. Zeng, Z. Zhou, P. Zhai, L. Zhang and H. Peng, *Nat. Protoc.*, 2024, **19**, 1557–1589.
5 C. P. Grey and D. S. Hall, *Nat. Commun.*, 2020, **11**, 1–4.
6 F. Duffner, N. Kronemeyer, J. Tübke, J. Leker, M. Winter and R. Schmuch, *Nat. Energy*, 2021, **6**, 123–134.
7 J. T. Frith, M. J. Lacey and U. Ulissi, *Nat. Commun.*, 2023, **14**, 420.
8 J. L. Guelfo, P. L. Ferguson, J. Beck, M. Chernick, A. Doria-Manzur, P. W. Faught, T. Flug, E. P. Gray, N. Jayasundara and D. R. U. Knappe, *Nat. Commun.*, 2024, **15**, 5548.
9 D. Han, C. Cui, K. Zhang, Z. Wang, J. Gao, Y. Guo, Z. Zhang, S. Wu, L. Yin, Z. Weng, F. Kang and Q. H. Yang, *Nat. Sustainability*, 2021, **5**, 205–213.
10 Q. Cao, Y. Gao, J. Pu, X. Zhao, Y. Wang, J. Chen and C. Guan, *Nat. Commun.*, 2023, **14**, 641.
11 R. Zhang, H. Xu, H. Dou and X. Zhang, *Adv. Funct. Mater.*, 2024, **15**, 2416497.
12 H. Wang, L. Zhao, H. Zhang, Y. Liu, L. Yang, F. Li, W. Liu, X. Dong, X. Li and Z. Li, *Energy Environ. Sci.*, 2022, **15**, 311–319.
13 H. Xu, R. Zhang, D. Luo, J. Wang, H. Dou, X. Zhang and G. Sun, *ACS Nano*, 2023, **17**, 25291–25300.
14 Y. Zhao, Y. Li, J. Mao, Z. Yi, N. Mubarak, Y. Zheng, J.-K. Kim and Q. Chen, *J. Mater. Chem. A*, 2022, **10**, 14090–14097.
15 C. Prehal, H. Fitzek, G. Kothleitner, V. Presser, B. Gollas, S. A. Freunberger and Q. Abbas, *Nat. Commun.*, 2020, **11**, 4838.
16 H. Wu, J. Hao, S. Zhang, Y. Jiang, Y. Zhu, J. Liu, K. Davey and S. Z. Qiao, *J. Am. Chem. Soc.*, 2024, **146**, 16601–16608.
17 J. Hao, S. Zhang, H. Wu, L. Yuan, K. Davey and S. Z. Qiao, *Chem. Soc. Rev.*, 2024, **53**, 4312–4332.
18 D. Lin and Y. Li, *Adv. Mater.*, 2022, **34**, 2108856.
19 R. Zhang, H. Xu, D. Luo, J. Wang, H. Dou and X. Zhang, *Energy Storage Mater.*, 2024, **67**, 103294.
20 H. Yu, Z. Wang, R. Zheng, L. Yan, L. Zhang and J. Shu, *Angew. Chem., Int. Ed.*, 2023, **62**, e202308397.
21 L. Zhang, M. Zhang, H. Guo, Z. Tian, L. Ge, G. He, J. Huang, J. Wang, T. Liu, I. P. Parkin and F. Lai, *Adv. Sci.*, 2022, **9**, 2105598.
22 S. J. Zhang, J. Hao, H. Li, P. F. Zhang, Z. W. Yin, Y. Y. Li, B. Zhang, Z. Lin and S. Z. Qiao, *Adv. Mater.*, 2022, **34**, 2201716.
23 J. He, H. Hong, S. Hu, X. Zhao, G. Qu, L. Zeng and H. Li, *Nano Energy*, 2024, **119**, 109096.
24 X. Yang, H. Fan, F. Hu, S. Chen, K. Yan and L. Ma, *Nano-Micro Lett.*, 2023, **15**, 126.
25 S. Yang, X. Guo, H. Lv, C. Han, A. Chen, Z. Tang, X. Li, C. Zhi and H. Li, *ACS Nano*, 2022, **16**, 13554–13572.

26 M. Liu, Q. Chen, X. Cao, D. Tan, J. Ma and J. Zhang, *J. Am. Chem. Soc.*, 2022, **144**, 21683–21691.
27 L. Ma, Y. Ying, S. Chen, Z. Huang, X. Li, H. Huang and C. Zhi, *Angew. Chem., Int. Ed.*, 2021, **60**, 3791–3798.
28 P. Vanýsek and L. Basáez Ramírez, *J. Chil. Chem. Soc.*, 2008, **53**, 1455–1463.
29 P. Navalpotro, N. Sierra, C. Trujillo, I. Montes, J. Palma and R. Marcilla, *ACS Appl. Mater. Interfaces*, 2018, **10**, 41246–41256.
30 J. Meng, Q. Tang, L. Zhou, C. Zhao, M. Chen, Y. Shen, J. Zhou, G. Feng, Y. Shen and Y. Huang, *Joule*, 2020, **4**, 953–966.
31 A. F. Molina Osorio, A. Gamero Quijano, P. Peljo and M. D. Scanlon, *Curr. Opin. Electrochem.*, 2020, **21**, 100–108.
32 R. M. Lynden Bell, R. Kosloff, S. Ruhman, D. Danovich and J. Vala, *J. Chem. Phys.*, 1998, **109**, 9928–9937.
33 F. S. Zhang and R. M. Lynden Bell, *Eur. Phys. J. D*, 2005, **34**, 129–132.
34 G. Manca, A. Ienco and C. Mealli, *Cryst. Growth Des.*, 2012, **12**, 1762–1771.
35 C. J. Margulis, D. F. Coker and R. M. Lynden Bell, *Chem. Phys. Lett.*, 2001, **341**, 557–560.
36 J. P. Cerón Carrasco, D. Jacquemin, C. Laurence, A. Planchat, C. Reichardt and K. Sraïdi, *J. Phys. Org. Chem.*, 2014, **27**, 512–518.
37 H. A. Benesi and J. H. Hildebrand, *J. Am. Chem. Soc.*, 1949, **71**, 2703–2707.
38 M. Telfah, A. A. Ahmad, A. M. Alsaad, Q. M. Al-Bataineh and A. Telfah, *Polym. Bull.*, 2022, **79**, 10803–10822.
39 H. Naorem and S. D. Devi, *Spectrochim. Acta, Part A*, 2013, **101**, 67–73.
40 J. Ma, M. Liu, Y. He and J. Zhang, *Angew. Chem., Int. Ed.*, 2021, **60**, 12636–12647.
41 D. Li, T. Xia, W. Feng and L. Cheng, *RSC Adv.*, 2021, **11**, 32852–32860.
42 H. Wang, X. Liu, J. Zhong, L. Du, S. Yun, X. Zhang, Y. Gao and L. Kang, *Small*, 2024, **20**, 2306947.
43 A. C. Hayes, P. Kruus and W. A. Adams, *J. Solution Chem.*, 1984, **13**, 61–75.
44 I. Rey, J. C. Lassègues, J. Grondin and L. Servant, *Electrochim. Acta*, 1998, **43**, 1505–1510.
45 D. Zhao, Q. Zhu, Q. Zhou, W. Zhang, Y. Yu, S. Chen and Z. Ren, *Energy Environ. Mater.*, 2024, **7**, e12522.
46 Q. Deng, F. Liu, X. Wu, C. Li, W. Zhou and B. Long, *J. Energy Chem.*, 2024, **89**, 670–678.
47 M. Prabakaran, S. Ramesh and V. Periasamy, *J. Adhes. Sci. Technol.*, 2016, **30**, 24–44.
48 Z. Hou, M. Dong, Y. Xiong, X. Zhang, H. Ao, M. Liu, Y. Zhu and Y. Qian, *Small*, 2020, **16**, 2001228.
49 J. Zou, G. Wang, S. Lin, H. Yang, X. Ma, H. Ji, S. Zhu, Y. Lyu, C. Wang and Y. Zhou, *Adv. Funct. Mater.*, 2024, **34**, 2415607.
50 X. Hu, Z. Zhao, Y. Yang, H. Zhang, G. Lai, B. Lu, P. Zhou, L. Chen and J. Zhou, *InfoMat*, 2024, **6**, e12620.
51 L. Zhang, H. Ding, H. Gao, J. Gong, H. Guo, S. Zhang, Y. Yu, G. He, T. Deng and I. P. Parkin, *Energy Environ. Sci.*, 2025, **18**, 2462–2473.
52 K. Zhang, Y. Ge, Q. Yu, P. Zhang, Y. Feng, Z. Tie, J. Ma and Z. Jin, *Energy Storage Mater.*, 2024, **67**, 103296.